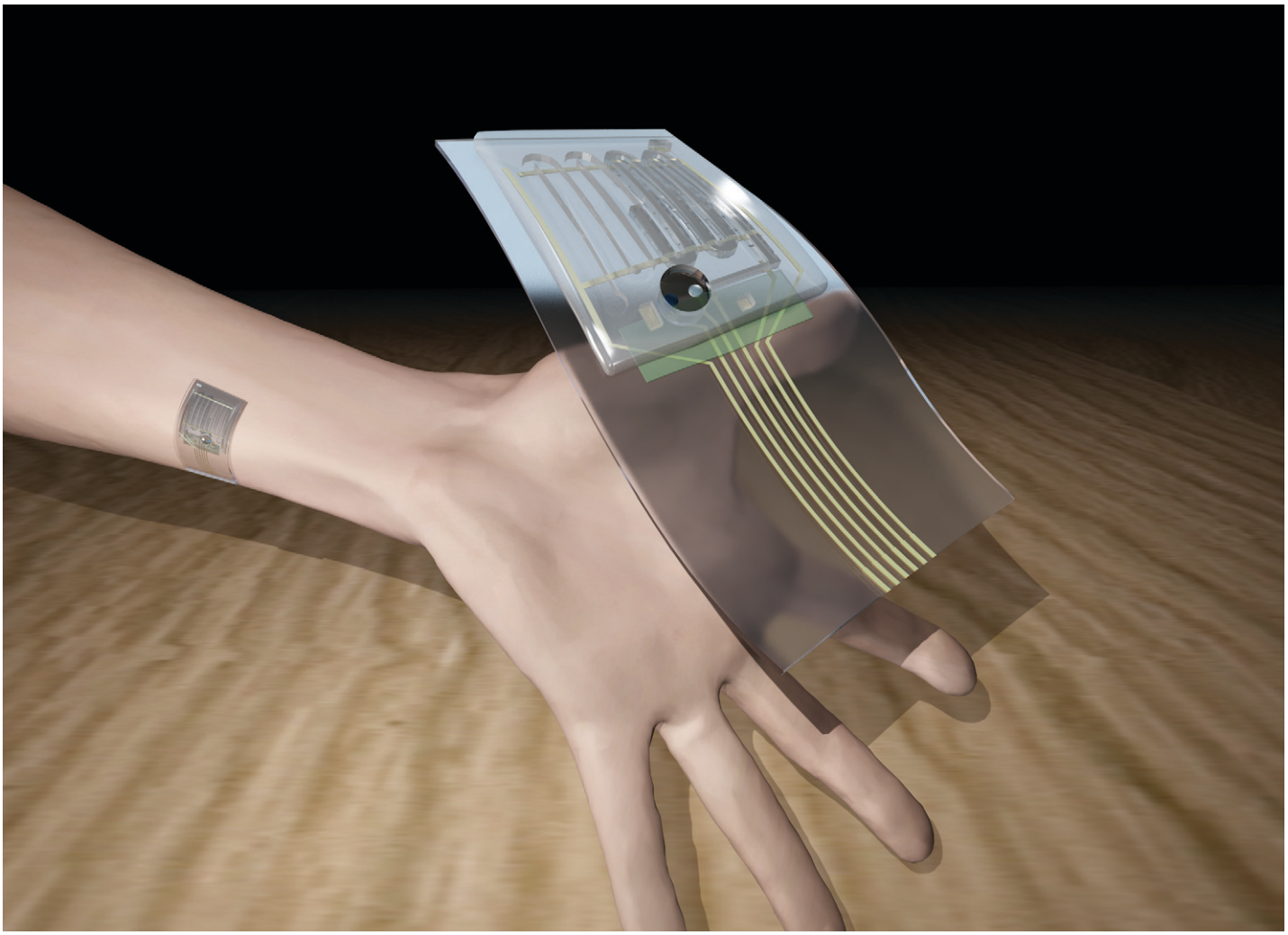

Featuring work from Professor Ali Javey's laboratory, Department of Electrical Engineering and Computer Science, University of California, Berkeley, USA.

A multi-modal sweat sensing patch for cross-verification of sweat rate, total ionic charge, and Na^+ concentration

A wearable sweat sensor uses interdigitated electrode fingers in a sweat-collecting microfluidic channel to produce admittance jumps that can be efficiently counted for selective sweat rate estimation. With integration of an impedimetric sensor for measuring total ionic charge concentration and an electrochemical Na^+ sensor, the overall multi-modal system enables cross-verification across sensor signals for reliable sweat analysis.

As featured in:

See Ali Javey *et al.*, *Lab Chip*, 2019, **19**, 3179.

ROYAL SOCIETY OF CHEMISTRY | Celebrating IYPT 2019

rsc.li/loc

Registered charity number: 207890

Lab on a Chip

PAPER

View Article Online
View Journal | View Issue

Cite this: *Lab Chip*, 2019, **19**, 3179

A multi-modal sweat sensing patch for cross-verification of sweat rate, total ionic charge, and Na^+ concentration†

Zhen Yuan,‡[abc] Lei Hou,‡[abc] Mallika Bariya, ‡[abc] Hnin Yin Yin Nyein,[abc] Li-Chia Tai,[abc] Wenbo Ji,[abc] Lu Li[abc] and Ali Javey*[abc]

Sweat sensors introduced in recent years have targeted a variety of sweat features and biomarkers for non-invasive health monitoring. Amongst these targets, reliable monitoring of sweat rate is crucial due to its modulation of sweat analyte concentrations and its intrinsic significance to numerous medical and physiological health conditions. Here we present a sweat rate sensor structure comprising of electrodes with interdigitated fingers in a microfluidic channel. Each time the accumulating sweat impinges on an electrode finger, the sensor reports a jump in admittance that can be simply and efficiently counted to estimate sweat rate, overcoming selectivity limitations of previously reported sweat rate sensors. We further integrate an impedimetric sensor for measuring total ionic charge concentration and an electrochemical Na^+ sensor, together creating a multi-modal system for analyzing fluid and electrolyte secretion. We demonstrate how low analyte diffusion rates through this microfluidic device allow for multi-purpose sensor function, including utilizing the sweat rate sensor signal to corroborate total ionic sensor measurements. This cross-verification capability ensures data integrity in real time, satisfying a vital consideration for personalized healthcare technologies. We use the presented patch for continuous analysis of sweat rate, total ionic charge concentration, and Na^+ concentration during exercise, while demonstrating how multi-modal cross-verification brings new trust to sensor readings.

Received 20th June 2019,
Accepted 18th August 2019

DOI: 10.1039/c9lc00598f

rsc.li/loc

Introduction

Amidst a growing shift towards personalized health care, wearable and point-of-care devices play a crucial role in diagnostics and monitoring of human health and fitness.[1–16] These devices include sensors that track physical parameters like heart rate and blood pressure,[8] as well as chemical sensors cast in test strip or implantable form factors for monitoring disease biomarkers like glucose in blood.[17] More recently, wearable devices have been developed that measure biomarkers in sweat.[3,5–7,14–16,18] Sweat is an attractive biofluid for point-of-care health monitoring as it can be accessed non-invasively at convenient body locations and contains diverse biomarkers and parameters that could potentially reflect the health of the body. For instance, the rate of sweating could indicate hydration status and total body fluid loss,[19,20] as well as neurological damage in stroke victims and patients.[21] The total ionic concentration of sweat is a marker of diseases like cystic fibrosis and can indicate the body's overall electrolyte homeostasis,[22] crucial to maintaining muscle performance during exercise.[23] Further, monitoring specific components of sweat, such as individual ions or metabolites, could provide detailed information on functions and metabolic pathways in the body.[3,5,6] Compact, wearable devices for multiplexed measurement of such sweat parameters can therefore be useful for monitoring dynamic changes in the chemical state and physiology of the body. In this work, we integrate impedimetric and electrochemical sensors into a unified device for reliable, cross-verified measurement of sweat secretion rate, total ionic charge concentration, and Na^+ concentration. While sensors of varying modalities have been demonstrated previously for sweat sensing, few reported devices integrate multiple detection modes into a single device. Uniting different modes and comparing signal redundancies or overlaps between sensors can be used to ensure integrity of sensor measurements. This is a vital consideration for healthcare-oriented wearables, for which sensor measurements must have the utmost reliability in order to relay actionable physiological information.

[a] *Department of Electrical Engineering and Computer Sciences, University of California, Berkeley, California 94720, USA. E-mail: ajavey@eecs.berkeley.edu*
[b] *Berkeley Sensor and Actuator Center, University of California, Berkeley, California 94720, USA*
[c] *Materials Sciences Division, Lawrence Berkeley National Laboratory, Berkeley, California 94720, USA*

† Electronic supplementary information (ESI) available: Fig. S1–S13 are referenced in the paper. See DOI: 10.1039/c9lc00598f

‡ These authors contributed equally.

In this work, sensors are nested within a serpentine microfluidic channel for real-time, multi-modal sweat analysis (Fig. 1). The impedimetric sweat rate sensor comprises of two electrodes with interdigitated fingers over which the serpentine channel repeatedly passes. Each time fluid accumulating in the channel impinges on another electrode finger, the admittance measured between the electrodes discretely jumps. As these jumps occur when sweat has reached specific positions within the channel, the distance between electrode fingers can be divided by the time between the admittance jumps to quantify sweat rate. The actual magnitude of the admittance jump is set by the conductivity of the oldest captured sweat, which constitutes the front of the sweat column that is flowing in the channel and making new connections between electrode fingers. Because of the discrete nature of this measurement scheme, in which admittance jumps occur at well-defined distances within the channel and thus depend solely on sweat rate, this sensor overcomes the selectivity issues of previously reported, continuous sweat rate sensors.[14,24] Specifically, a sweat rate sensor previously reported by our group measures impedance magnitude between immersed metal electrodes and is therefore influenced by both sweat volume and sweat ion composition. In this work, by constructing a novel sensor architecture that considers sudden changes in impedance rather than impedance magnitude directly, we can isolate the effect of sweat volume to measure sweat rate with new selectivity. This isolation is enabled because physiological sweat ion changes occur over minutes, so dramatic changes in impedance that occur over seconds can accurately be ascribed to a new electrode finger being crossed, signifying the distance sweat has traveled for direct, accurate conversion to sweat rate. Further, the regular, repeating pattern of the microfluidic channel crossing the electrode fingers ensures that these crossings are made regularly per a set amount of fluid entering the channel. This makes for simpler and more resolved sweat rate extraction compared to when using variable electrode finger separation or continuous impedimetric sensing.

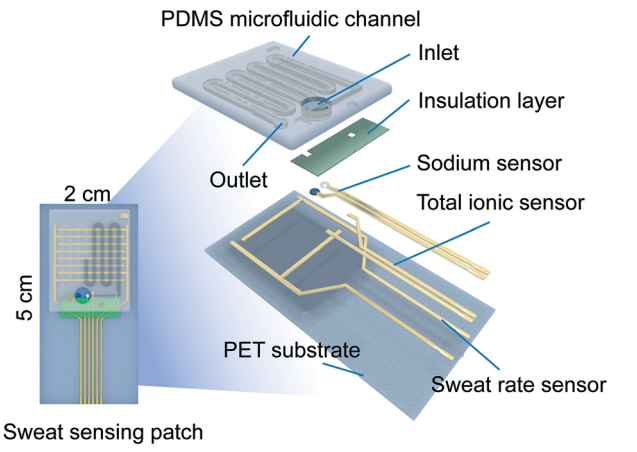

Fig. 1 Schematic of multi-modal sweat sensing patch with sensors for sweat rate, total ionic charge concentration, and Na^+ ion concentration located within a PDMS microfluidic for sweat capture and flow.

While discontinuous jumps in admittance can accurately reflect sweat rate, the sweat rate sensor signal can drift in the interim between admittance jumps. This drifting is due to conductivity changes of the accumulating sweat. Specifically, deltas in admittance between consecutive sweat rate sensor measurements are determined by the conductivity, or total ionic charge concentration, of the sweat volume that most recently entered the channel (note that this conductivity includes total charge magnitude contributions from all ionic species, not net charge). Analyzing this differential portion of the sweat rate sensor signal can therefore be used to verify the total ionic charge sensor reading. The total ionic charge sensor comprises of two impedimetric electrodes located near the entry point of the microfluidic channel to measure conductivity of the freshest sweat (Fig. 1). This is an important new addition to the growing library of sweat sensors as the ionic charge composition of sweat is significant for health conditions like cystic fibrosis or stroke[21,25] and in exercise physiology. Overall, we present two modalities for measuring total ionic charge concentration: modality 1 involves using the total ionic charge sensor to measure sweat conductivity directly, which modality 2 utilizes the differential admittance signal from the sweat rate electrodes and can be used to cross-check the measurements from modality 1. Modality 2 is conceptually described in Fig. 2, in which fluid with a model ionic concentration gradient is shown schematically flowing through the channel (Fig. 2(a)). In the sweat rate electrode admittance signal, a discrete step occurs when fluid makes a new connection between electrode fingers as shown in Fig. 2(b). In contrast, drift or variation in the sensor signal within the relatively flat portion of a step comes from ionic charge variation in the fluid when it only partially fills the region between fingers. The sweat rate sensor signal is differentiated (Fig. 2(c)) such that spikes in the differential signal correspond to sweat rate while the non-spike background admittance is due to total ionic charge. By setting a threshold value filter to identify and subtract out spikes, the two signals can be separated. While the differential admittance signal spikes can be reconstructed into sweat rate (Fig. 2(d)), the background admittance signal is re-integrated to give an admittance profile arising solely from the fluid's ionic concentration gradient (Fig. 2(e)) and calibrated into a measure of total ionic concentration. While this is a conceptual overview of modality 2 and how it can be used to verify the total ionic sensor reading, in reality certain criteria must be met in order to use this method reliably. These criteria include being able to linearly add admittance contributions from different portions of fluid and having minimal ion mixing or diffusion within the channel. We will demonstrate further on how these criteria are met.

As sodium ions typically make up the majority of the electrolyte composition of sweat, the total ionic charge sensor can in turn be used to verify the Na^+ sensor reading,[26] specifically by confirming that the Na^+ sensor reading is similar to

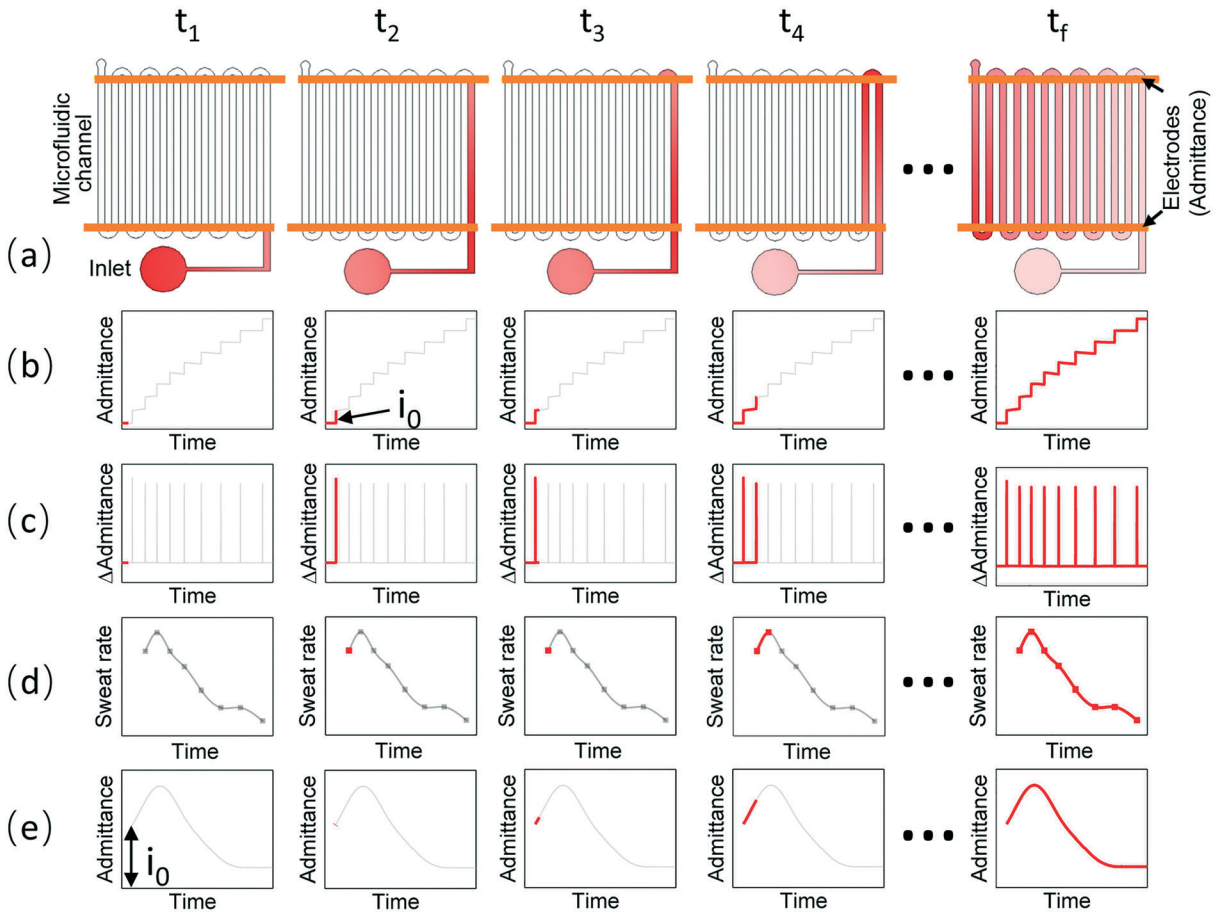

Fig. 2 Schematic representation of how dynamic sweat rate and total ionic concentration measurements are made using the sweat rate electrodes. (a) Schematic of fluid filling the serpentine microfluidic channel from time t_1 to t_f. Sweat rate electrode fingers are shown in yellow. A model ionic concentration gradient is indicated by the color gradient. (b) Corresponding admittance signal recorded between the sweat rate electrodes over time is shown in red. A step occurs each time fluid makes a new connection between the sweat rate electrode fingers. Step height i_0 is determined by conductivity of the leading column of fluid. (c) Differential admittance signal. Spike occurs in response to fluid makes a new connection between the sweat rate electrode fingers. The non-spike, background portion of the signal constitutes the drift within each admittance step shown in b. (d) As the spacing between electrode fingers is known, this intervening volume can be divided by the time between differential admittance signal spikes to reconstruct sweat rate. (e) Background portion of the admittance signal from b is re-integrated into the admittance profile arising from the fluid's ionic concentration gradient, and can be calibrated into a measure of total ionic concentration. This is referred to as modality 2 for total ionic sensing.

but never greater than the total ionic sensor reading. The Na^+ sensor comprises of an ion-selective electrode and an Ag/AgCl reference electrode located in the microfluidic entry well. The open-circuit potential measured between the two is linearly related to sodium ion concentration. While each sensor of this patch targets a different feature of sweat, the interdependencies between the sensor readings, established through intrinsic chemical relations between targets and through electrode structure design, allow the sensor readings to be cross-verified for enhanced reliability. While previously reported devices have occasionally attempted to ensure reliability using multiple copies of the same sensor, using a multi-modal approach overcomes issues of bias or influence that could affect all copies of the same sensor. In this way, the presented multi-modal device represents a reliable sensing platform for sweat analysis with in-built schemes of signal verification.

Below, we first characterize the sweat rate, total ionic charge, and Na^+ sensors. We then investigate electrolyte diffusion kinetics within the channel, as diffusion effects can impact whether sensor readings are accurate and real-time. We show that this diffusion is slow compared to typical durations of sweat analysis, which not only ensures real-time sensing but also crucially allows the sweat rate sensor to be used for cross-verification of the total ionic charge sensor. Finally, we demonstrate this system for *in situ* sweat analysis during stationary biking to track real-time profiles of sweat parameters towards health and fitness applications.

Results and discussion

Structure of the multi-modal sweat sensing patch

The patterned Au electrodes constituting the sweat rate sensor, total ionic charge sensor, and Na^+ sensor base layers are

fabricated *via* photolithography on flexible polyethylene terephthalate (PET) substrate. The serpentine microfluidic channel is prepared through polydimethylsiloxane (PDMS) molding and chemically bonded to the PET substrate in order to enclose the sensing electrodes within the microfluidic channel or its entry reservoir. The channel is 1 mm in width and 100 μm in height (Fig. S1†), and the reservoir has a 3 mm diameter for sweat to first collect and impinge on the Na^+ and total ionic charge sensors before pushing into the channel. The microfluidic reservoir and channel have a total volume capacity of ~15 μl, allowing for over an hour of on-body sweat collection and measurement at typical exercise sweat rates on the order of 0.2 μl min^{-1}.[27] To accommodate for sweat rate measurements spanning greater time or volume of accumulated sweat, the channel length can be extended during fabrication to enable a greater number of crossings of the serpentine channel over the sweat rate electrode fingers. Even once the channel is filled with sweat, new sweat can continue to enter the reservoir and channel while pushing older sweat out of the microfluidic outlet, allowing the ion sensors in the reservoir to continue giving updated, real-time measurements in the freshest sweat. Note that the 'U-shape' turn of the microfluidic channel as it winds back over the sweat rate electrodes is designed to minimally extend beyond either electrode, to minimize the fluid volume whose ionic charge contribution is not accounted for in modality 2 (this 'U-shape' portion reconnects the same electrode, effectively shorting the fluid portion out of the admittance measurement). Further, to ensure accurate ionic charge measurements with modality 2, the sweat rate electrode finger widths are narrow compared to the intervening distance between electrodes to ensure minimal signal drift as sweat flows over the span of either electrode. The finger width is 0.5 mm compared to separation between electrodes of 12.0 mm, 4.3 mm, and 1.5 mm for electrodes with 1, 2, and 4 fingers respectively.

The flow of sweat into and through the device is powered by sweat gland fluid pressure which can reach up to 70 kPa per gland – sufficient to drive sweat into such soft, conformally worn microfluidic systems.[27] The overall patch is about 10 cm^2 for comfortable and conformal attachment as a wearable device (Fig. 1). As this device footprint is small enough to fit on the relatively flat inner forearm or forehead, and further as only the entry reservoir region must be tightly attached to enable sweat collection, the device does not endure significant bending and is robust for on-body use.

Sweat rate sensor operation and characterization

We first establish measurement parameters over which sweat rate sensor performance can then be characterized. Thermal stability of the sweat rate sensor across room and body temperatures, and its signal dependence on total ionic charge but invariance to specific electrolyte species, is reported in Fig. S2 and S3† respectively. Further, we show that fluid evaporation from the microfluidic channel is minimal across a range of temperatures and humidity levels (Fig. S4†). Based on these findings, sweat rate sensor characterization measurements are conducted at room temperature, ambient humidity around 50%, and using NaCl as a representative electrolyte due to its dominant concentration in sweat.[28] As test solutions have equal concentrations of cations and anions, and sweat is also a net neutral biofluid, we choose to translate admittance measurements simply into equivalent cation concentrations in all subsequent experiments. The impact of ionic charge concentration on the sweat rate sensor admittance value is analyzed by electrochemical impedance spectroscopy (EIS). EIS Nyquist plots over a 10 to 200 mM concentration range pertinent to sweat are plotted in Fig. S5.† The corresponding Bode phase plot shows that the phase variation over this range is minimized to 5° at a measurement frequency of 1 kHz. Because the total ionic charge concentration of sweat realistically changes over a tighter concentration range during exercise, this phase angle variation is expected to be even smaller during actual continuous sweat measurement.[16] For this reason, the sweat sensor admittance response can be treated as a linear system at 1 kHz. Specifically, the total measured admittance magnitude can be treated as a scalar sum of the admittance magnitude contributions of each volume of sweat within the channel, even when those volumes differ in ionic concentration. This linearity will be shown to be crucial for enacting cross-verification, and for this reason the sweat rate sensor is operated at 1 kHz in the following measurements.

The sweat rate sensor consists of two Au electrodes electrically connected when sweat impinges on the interdigitated electrode fingers within the microfluidic channel. The distance between the fingers determines the quantized sweat volume that must be added into the channel to detect a change in total volume *via* a jump in admittance (or *via* spikes in the differential signal, as in Fig. 3a). Therefore, smaller spacing between the electrode fingers, achieved by increasing the number of fingers, can be used to make sweat rate measurements with higher temporal resolution. Yet more fingers lead to lower noise tolerance when identifying admittance jumps (or differential signal spikes) as seen in Fig. S6.† The number of fingers should therefore be optimized between temporal and signal resolution for different applications, but for demonstration purposes a one-finger-per-electrode structure is representatively chosen for the subsequent device characterization.

The sweat rate sensor signal at different input flow rates is characterized in Fig. 3b using a solution of 50 mM NaCl. At higher flow rates injected by a syringe pump, the jumps in admittance occur more frequently in time. The magnitude of the jump is set by the conductivity of the oldest sweat in the channel, which is essentially unchanged with each jump at low enough diffusion rates (which will be shown further on to be the case for this device) even for fluid of dynamically varying concentration. By simply counting the rate of admittance jumps by considering when the time derivative of the admittance signal suddenly increases above a baseline threshold, we can estimate flow rate through the channel as

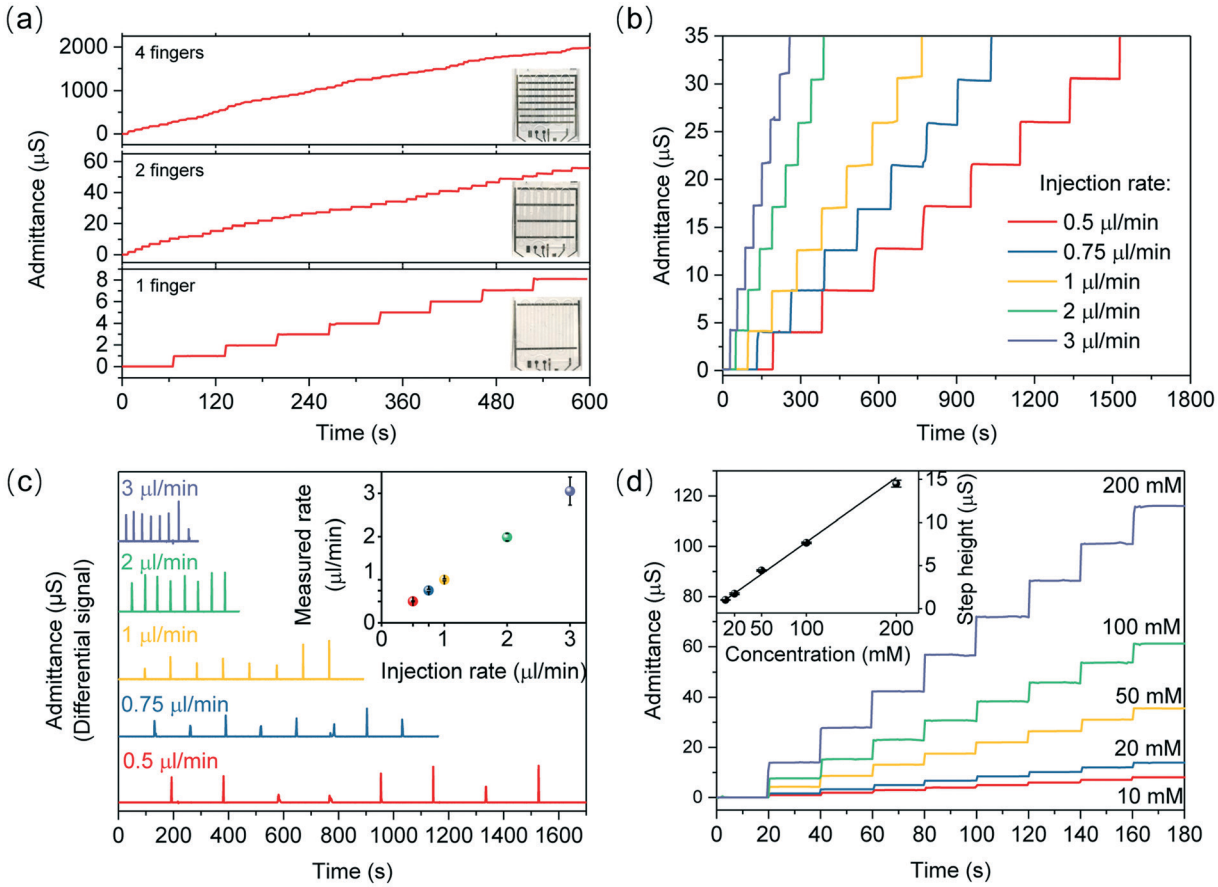

Fig. 3 Characterization of sweat rate sensor performance. (a) Admittance response to 50 mM NaCl injected at 1.45 μl min^{-1} for sensors with 1, 2, and 4 interdigitated electrode fingers. All following figures use 1 finger per electrode. (b) Admittance response to different injection rates of 50 mM NaCl solution. (c) Differential signal of sensor response at different injected flow rates, used to estimate the flow rate. Inset shows 1 : 1 correlation between true and measured flow rates. The inset points average over 8 measurements per injection rate, derived by monitoring 8 differential admittance signal spikes over time. Higher variation at higher flow rates stems from syringe pump precision limitations. (d) Sensor response to injected solutions of different NaCl concentrations, with inset calibration curve showing linear increase in admittance step height with concentration.

shown in Fig. 3c. The inset reveals that this measured flow rate coheres 1 : 1 with the true fluid injection rate inputted by the syringe pump. Fig. 3d shows the sweat rate sensor response to different concentrations of NaCl solution at a constant flow rate of 4.8 μl min^{-1}. While higher ionic concentrations of fluid in the channel increase the magnitude of the jumps in admittance, they do not impact the periodicity of the steps as this is uniquely determined by the spacing or number of electrode fingers. This highlights an advantage of this discreet sweat rate measurement scheme compared to previously reported, continuous sweat rate sensors. Here, counting spikes in the signal derivative gives an independent and robust sweat rate measurement that is unaffected by changes in the accumulating sweat's conductivity, even as the original, non-differentiated admittance signal captures useful information on sweat conductivity.

Total ionic charge and sodium sensor characterization

Unlike the sweat rate electrodes, which must consider the entire volume of captured sweat in order to make real-time measurements, the total ionic charge and Na^+ sensors are situated at the entry point of the microfluidic channel to access the freshest sweat for real-time analysis. The total ionic concentration of fresh sweat held in the entry reservoir impacts the conductivity measured between the metal lines of the total ionic charge sensor. The Na^+ concentration of this sweat is transduced by the selective ionophore membrane of the potentiostatic Na^+ sensor working electrode. The total ionic charge and Na^+ sensors are characterized in Fig. 4. The total ionic sensor shows consistent performance over 20 hours of continuous measurement in NaCl solution, with sensitivity of 0.063 μS mM^{-1} (Fig. 4(a)) and excellent stability (Fig. 4(b)). The sweat Na^+ sensor is characterized across 10 to 160 mM NaCl solution, though the sensor's stability and linearity extend beyond this range as seen in Fig. S7† and in previous work reported by our group.[3,29] The sensor gives repeatable response with negligible hysteresis when cycling over the different concentrations in Fig. 4c. Further, the sensor shows stable performance over 50 hours of continuous measurement, with near-Nernstian sensitivity of 57.17 mV per decade and drift lower than 2.8 mV h^{-1} as shown in Fig. 4d. To

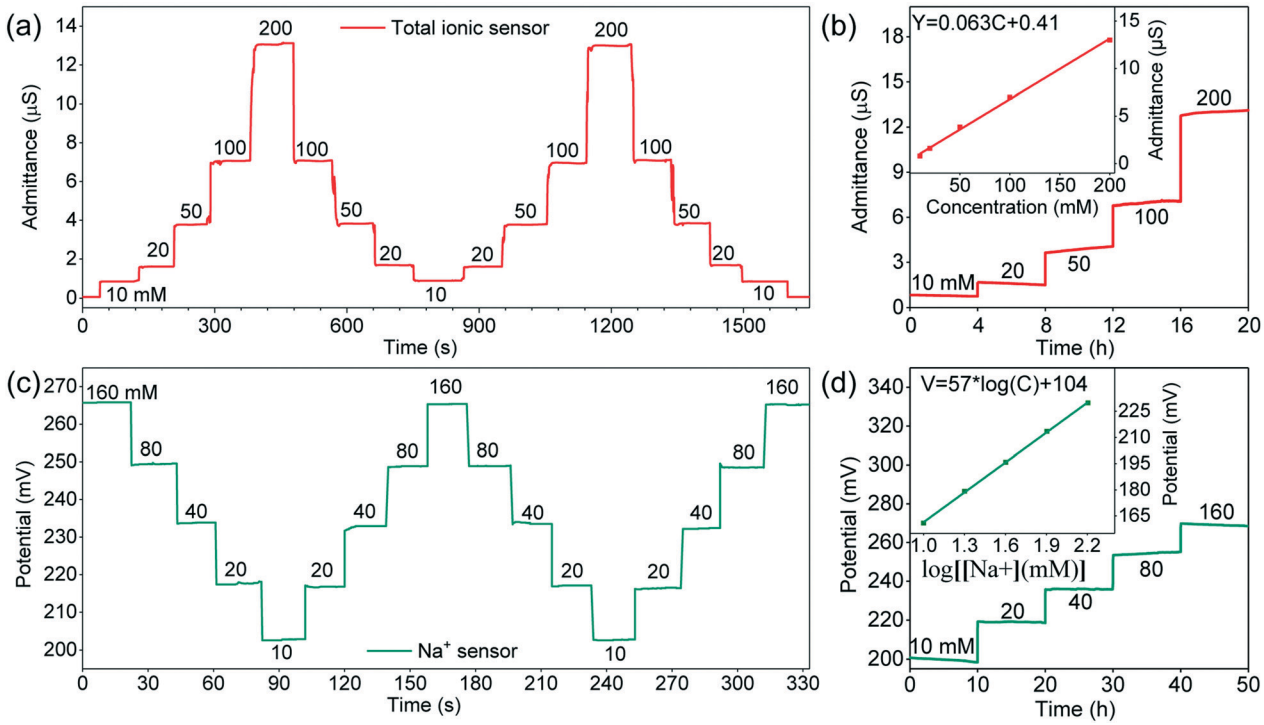

Fig. 4 Characterization of sensors for total ionic charge concentration and Na^+ concentration. (a) Repeatability of total ionic charge sensor cycled over solutions between 10 and 200 mM NaCl. (b) Stability of total ionic charge sensor over 20 hours of total measurement, with inset linear calibration curve with respect to NaCl concentration. (c) Repeatability of Na^+ sensor cycled between 10 and 160 mM NaCl. (d) Stability of Na^+ sensor over 50 hours of total measurement, with inset linear calibration curve with respect to NaCl concentration.

further demonstrate the independent and selective sensing performance of the total ionic charge and sodium sensors, solutions with different ion compositions are injected into the device at different flow rates, as shown in Fig. S8.† The total ionic sensor shows negligible dependence on flow rate, responding selectively to changes in total ionic concentration upon addition of Na^+, K^+, Mg^{2+}, or Ca^{2+} ions. The Na^+ sensor shows no significant response to changing flow rate or the addition of K^+, Mg^{2+}, or Ca^{2+} interfering ions but responds sensitively to changes in Na^+.

Cross-verification between modalities for determining total ionic concentration

Modality 2 for measuring total ionic concentration involves deconstructing the sweat rate electrodes' admittance signal to identify the contribution from ionic charge. This modality can be used to cross-verify modality 1, in which the total ionic sensor is used to measure ionic charge directly. To realize modality 2, the admittance contribution of the freshest sweat must be isolated. This contribution gives the conductivity of the freshest sweat and should match the total ionic charge sensor reading. As admittance contributions from portions of sweat add linearly at the 1 kHz measurement frequency, isolation of the freshest sweat's contribution is possible as long as there is slow electrolyte diffusion through the microfluidic channel. This ensures that the fresh sweat is intact upon reaching the sweat rate electrodes, without mixing with older sweat already in the channel. Such mixing does not just impact the sweat rate sensor, as high diffusion rates prevent all sensor readings from being truly real-time. In fact, no systematic investigation of diffusion effects on analyte profiles has been previously conducted for sensors utilizing microfluidic sweat capture. Here, we experimentally and theoretically characterize electrolyte diffusion through the device. First, water with different colored dye (green and red) is successively injected into the channel using a syringe pump and monitored for 1 hour to confirm that convective mixing is minimal (Fig. S9†) such that migration of electrolytes can only occur through diffusion. To determine diffusion rates, two volumes of NaCl solution with different concentrations (75 mM and 100 mM, with associated volumes false-colored purple and red respectively) are successively injected as shown in Fig. 5a, a close-up of the filled channel between the total ionic sensor and the sweat rate sensor. Based on Fick's second law ($\partial\varphi/\partial t = D(\partial^2\varphi)/(\partial x^2)$), the theoretical concentration distribution along the channel and over time is simulated in Fig. 5b. The temporal concentration profile is extracted from this theoretic distribution at the two channel positions marked light and dark green (Fig. 5c), encompassing the fluid segment between the first channel crossing of the sweat rate electrode fingers. The average ionic concentration of the fluid between these points can be experimentally measured for comparison *via* the admittance signal from the sweat rate electrode. (Fig. 5c). Since the measured admittance indicates the average ion concentration between the fingers, the profiles from the light and dark green points are also averaged for

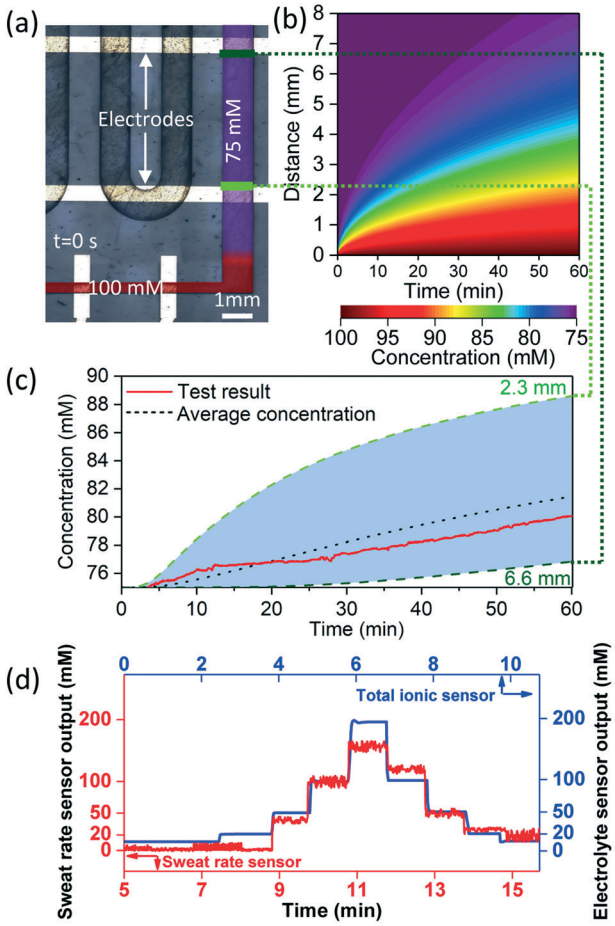

Fig. 5 Ion diffusion analysis within the microfluidic channel. (a) Optical, false-color image of microfluidic channel segment adjacent to the entry reservoir and containing NaCl solution. Fluid within the channel of 74 mM NaCl is false-colored purple; fluid of 100 mM is false-colored red. (b) Temporal ion concentration profiles are simulated across points within the channel using Fick's law of diffusion. Vertical axis in the simulation aligns with position along the channel in the optical image. (c) Simulated temporal profiles are extracted at positions marked dark and light green (located at 6.6 and 2.3 mm from the solution interface respectively) along the channel and used to estimate average concentration between the sweat rate electrodes (dashed line). Measured concentration based on admittance signal of sweat rate electrodes is shown in red and closely matches the theoretical profile. (d) Measured total ionic charge concentration (blue), and estimated total ionic charge concentration from the sweat rate sensor signal (red) are compared as different concentration of NaCl solution are injected into the channel.

comparison. These experimentally and theoretically derived profiles are in close agreement, with predicted and measured concentrations differing by less than 2 mM. This discrepancy can be attributed to small errors in precisely locating the interface between the two fluidic segments of different concentrations, an input for the simulation. As shown in Fig. 5c, the concentration response changes by just 7% after one hour and is expected to be lower for true sweat analysis which typically involves less dramatic concentration gradients. This finding indicates that ion diffusion only slightly alters the electrolyte content of a fresh volume of sweat during typical measurement times, indicating that the sweat sensors united in this device can give accurate and real-time readings with minimal influence of mixing and diffusion. It further ensures that the admittance contribution of newly captured sweat can be reliably isolated from the remaining sweat regarding the sweat rate sensor signal, allowing cross-verification of conductivity measurements as described next.

Based on low diffusion rates preserving local electrolyte concentrations, we demonstrate using the sweat rate electrodes to cross-verify the total ionic charge sensor reading in Fig. 5d. Solutions with different NaCl concentration were injected into the device. Due to scalar addition of admittance contributions, we can subtract the previous admittance reading from the current reading to isolate the differential admittance contribution of the most recent sweat and use this to reconstruct the total ionic charge signal, following the procedure detailed in Fig. 2. Note that as the injection rate of Fig. 5d is around 0.2 μl min^{-1}, the initial sweat volume to first enter the microfluidic will have a delay of about 5 min between impinging on the total ionic charge sensor and filling the first column of the sweat rate sensor, creating a 5 min delay between the profiles obtained *via* modality 1 and modality 2. Thus, the time axis is shifted by 5 min for modality 2 in Fig. 5d for convenience. The resulting profiles from modalities 1 and 2 show similar trends – when the total ionic sensor shows a sharp signal increase in response to newly injected solution of higher concentration, the profile derived from the sweat rate electrodes shows a corresponding sharp increase. Discrepancies arise from imprecise manual injection of constant volumes, causing adjacent volumes of different concentrations to partially occupy the region between electrode fingers simultaneously. This causes a slight underestimation of higher concentration volumes and a subsequent overestimation of lower concentration volumes. However, this error is a result of manual fluid injection and is expected to be lower for real sweat analysis. The overall similarity between the profiles indicates that the sweat rate sensor can be used to independently verify the total ionic sensor data during the measurement process, allowing for continuous self-consistency checks that are important for establishing integrity of sensor data.

Device demonstration for on-body sweat analysis during exercise

To demonstrate the multi-modal sweat sensing patch *in situ*, the device was attached to 3 subjects' forearms during 6 trials of stationary, constant-load biking for exercise-based sweat generation. The experimental and instrumental set-up for these trials is shown in Fig. S10.† Trials 1 and 3 from subject A, trial 2 from subject B, and trial 4 from subject C are show in Fig. 6. Trial 5 from subject A and trial 6 from subject C are shown in Fig. S11.† Real-time profiles of sweat rate, total ionic charge concentration, and Na^+ concentration are shown for each trial in panels i–iv respectively. The raw sweat rate sensor admittance profiles shown in panels labeled i are differentiated to identify the signal spikes that indicate captured sweat volume (described in Fig. S12†) for conversion into real-time

sweat rate measurements in panels ii. Admittance steps are comparatively less smooth for trial 2 due to the subject's more rapidly changing ionic concentration during this trial, but note that the sudden jumps in admittance are still easily identifiable for sweat rate estimation. Sweat rate increases after the onset of perspiration for trials 1, 2, and 4 as expected based on previously reported trends.[14] It then decreases before eventually stabilizing after 10, 15, and 4 min respectively due to adaption and equilibration of the body's response to the biking load. Trial 3 shows a nearly constant sweat rate throughout. Panels labeled iii show total ionic charge profiles for each trial derived from modality 1 (solid red line) and modality 2 (dashed grey line). A 1-to-1 comparison of these modalities is shown in Fig. S13,† using data points sampled from on-body trials 1–6 (specifically, 20 data points sampled at regular intervals from each trial). The average discrepancy between the two methods across all trials is less than 10.0%. After compensating for the roughly 5-minute delay due to the offset positions of the sweat rate and total ionic electrodes, the modalities give comparable profiles as expected when the sensors are functioning correctly, highlighting the utility of multi-modal sensing in establishing sensor reliability. On-

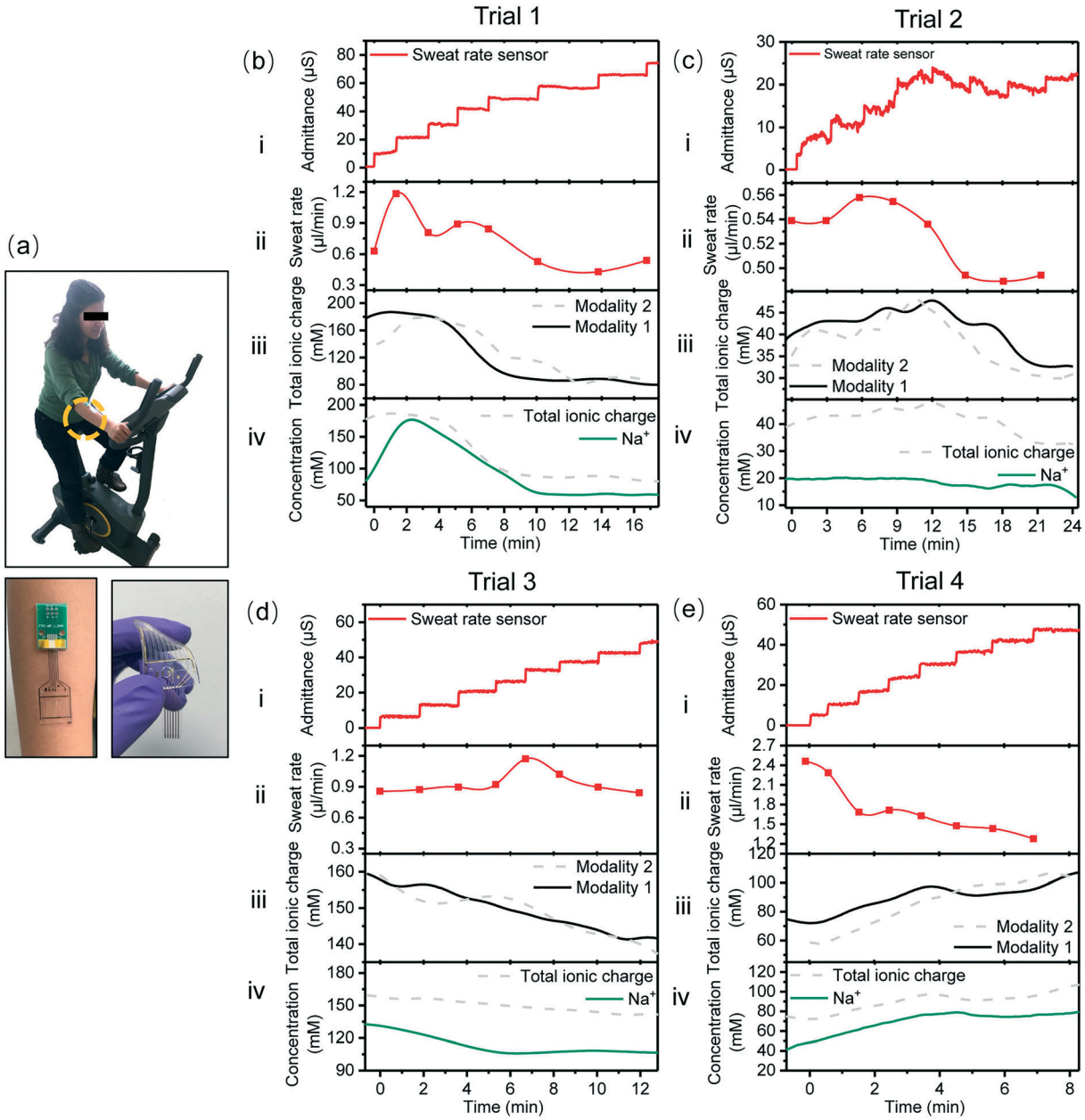

Fig. 6 Real-time, on-body sweat analysis during stationary biking exercise. (a) Optical image of subject with multi-modal sweat sensing patch affixed to their forearm, with connector board for signal read-out. (b)–(e) On-body sweat analysis trials 1–4 respectively, showing simultaneous measurement of (i) raw sweat rate sensor admittance data, (ii) sweat rate, (iii) total ionic charge concentration, and (iv) Na^+ concentration profiles. Trials 1 and 3 are conducted on subject A, trial 2 on subject B, and trial 4 on subject C.

body measurement of sweat Na^+ is shown in panels labeled iv (solid red line), along with the total ionic charge profile (dashed grey line) for rough comparison. For trial 1, the Na^+ concentration increases in the initial 3 min to a maximum near 180 mM and subsequently decreases along with the decreasing sweat rate before ultimately stabilizing around 60 mM (the sensing properties of sodium sensor in the range up to 200 mM is plotted as Fig. S7†).[16] In comparison, a slightly different trend and lower Na^+ values are observed in trial 2, which shows a slower concentration fall-off. The sodium Na^+ concentration in trial 3 keep decreasing during the test with the peak concentration of 132 mM at the beginning. For trial 4, along with the decreasing sweat rate, the Na^+ concentration gradually increased. As trials 1 and 2 show somewhat atypical sweat Na^+ concentrations outside the expected range of 56.7 ± 28.9 mM,[30] we verify the sweat ion concentrations of subjects A and B using traditional, off-body equipment. Specifically, sweat collected from the subjects and analyzed *via* inductively coupled plasma mass spectrometry (ICP-MS) are tested for Na^+ and K^+, typically the most dominant cations in sweat.[28] Subject A has 132.0 mM Na^+ and 12.6 mM K^+ concentrations, while subject B has 19.7 mM Na^+ and 17.2 mM K^+, with uncertainty of 0.4 mM and 0.3 mM for Na^+ and K^+ measurements respectively as given by the standard deviations of repeated ICP-MS calibration measurements in Na^+ and K^+ standard solutions. Na^+ is the dominant cation in the sweat of subject A, but is far less dominant for subject B who has an unusually high sweat K^+ content. This explains why, compared to subject A, the sweat Na^+ concentration for subject B is a much smaller fraction of the total ionic charge concentration as seen by comparing curves in panel iv of trial 1 and 2. The distinct temporal Na^+ trends demonstrated for the different subjects and trials can be attributed to a variety of factors, including differences in sweat secretion pathways and metabolism, diet, environmental conditions and heat acclimation. Overall, the profiles recorded during the on-body sweat trials shown in Fig. 6 demonstrate how the real-time, multi-modal signal verification scheme encoded by this device structure can be used to ensure integrity of sensor measurements. Moreover, while each sensor relays important information that could potentially be used to monitor dehydration and physiology during exercise, considering the multi-modal sensors together can further relay emergent information such as unexpected imbalances in traditional electrolyte ratios.

Conclusion

In this work, we demonstrate a wearable, multi-modal sweat sensing patch that simultaneously measures sweat rate, total ionic charge concentration, and Na^+ concentration for health and exercise physiology applications. The device structure enables real-time cross-verification of sensor signals, an important feature that allows the integrity of sensor readings to be continuously interrogated. We introduce an impedimetric sweat rate sensor with interdigitated electrode fingers that enable simple counting of admittance jumps to estimate sweat rate. Portions of the sweat rate sensor signal can be isolated to indicate sweat conductivity, allowing the total ionic sensor signal to be corroborated. This total ionic sensor consists of a pair of impedimetric electrodes located at the entry of the microfluidic channel, allowing real-time measurement of sweat electrolyte loss while also supporting cross-verification of the potentiometric Na^+ sensor reading. We further theoretically and experimentally investigate diffusion within the microfluidic sweat collector, finding that diffusion rates are low enough to ensure sensors give real-time measurements and can support the cross-verification scheme. We finally use this patch for real-time sweat analysis during stationary cycling, showing how multi-modal sensors united into a common platform can enhance sweat sensor integrity and even relay emergent health information such as unexpected imbalances in electrolyte ratios. The presented device demonstrates a crucial scheme for ensuring new trust in sensor data, a key translational consideration for making wearable sweat sensors reliable for real-world health monitoring applications.

Experimental

Materials

Selectophore grade sodium ionophore X, (3-aminopropyl)-triethoxysilane (APTES), bis(2-ethylehexyl) sebacate (DOS), sodium tetrakis [3,5-bis(trifluoromethyl)phenyl]borate (Na-TFPB), tetrahydrofuran (inhibitor-free), polyvinyl chloride (PVC, high-molecular weight), cyclohexanone, sodium chloride (NaCl), potassium chloride (KCl), magnesium chloride ($MgCl_2$), calcium chloride ($CaCl_2$), polyvinyl butyral resin BUTVAR B-98 (PVB), 3,4-ethylenedioxythiophene (EDOT), and poly(sodium 4-styrenesulfonate) (NaPSS) were purchased from Sigma-Aldrich. The polydimethylsiloxane (PDMS, Sylgard 184) was bought from Ellsworth Adhesives. Moisture-resistant 100 μm-thick PET was purchased from McMaster Carr.

Multi-modal sweat sensing patch fabrication

The electrodes were patterned on PET substrate through photolithography (Shipley Microposit S1818 photoresist) followed by evaporation of Cr/Au layers (30/80 nm). A 600 nm Parylene-C insulation layer was then deposited using SCS Labcoter 2 Parylene Deposition System. The Na^+ sensor was prepared through functionalizing working electrode and reference electrode according to our reported works with minor modifications. Working electrode was prepared by dropping 10 μl of the Na^+-selective membrane cocktail (1% Na ionophore X, 0.55% Na-TFPB, 33% PVC and 65.45% DOS in inhibitor-free tetrahydrofuran) onto the electrodes. 10 μl of reference solution (79.1 mg PVB and 40 mg of NaCl into 1 ml methanol) was dropped onto the Ag/AgCl electrode as the reference electrode. Then, the patterned device on PET substrate was treated with O2 plasma and APTES, successively prior to bonding to the PDMS microfluidic. The microfluidic channel was made using the template method. The serpentine mold was prepared with SU-8 photoresist (2075, MicroChem) through photolithography on a silicon wafer. PDMS was

homogeneously mixed at 10 : 1 weight% ratio of base : curing agent and degassed under vacuum for 1 hour. Degassed PDMS was poured onto the patterned SU-8 mold and cured for 1 hour at 90 °C. The cured PDMS microfluidic was peeled from the silicon wafer after cooling down. The inlet and outlet holes were punched out before the molded PDMS was treated with O2 plasma and bonded to the APTES-treated PET substrate.

Sensor characterization and off-body measurement

The admittance signals of the sweat rate and total ionic charge sensors were acquired using Keysight E4980AL LCR meters. All off-body measurements were obtained using NaCl solutions of various concentrations. Controlled flow rate experiments were carried out using Harvard Apparatus PHD 2000 Syringe Pump. The Na^+ sensor was characterized using CHI 1430 with a two-electrode system.

On-body sweat analysis during exercise

On-body human trials were carried out at the University of California, Berkeley in compliance with the human research protocol (CPHS 2014-08-6636) approved by the Berkeley Institutional Review Board (IRB). Two on-body trials were performed to demonstrate sensor function and accuracy. An electronically braked leg-cycle ergometer (Kettler E3 Upright Ergometer Exercise Bike) was used for stationary cycling trials. Subjects' wrists were wiped and cleaned with alcohol swabs and gauze before attaching the sensing patch with adhesive tape. The sweat rate response was acquired using Keysight E4980AL LCR meters. The total ionic sensor measurements were acquired using Gamry potentiostat. CHI 1430 potentiostat was used to acquire Na^+ sensor data. Na^+ sensors used for on-body measurement were pre-calibrated before being bonded to the PDMS layer and packaged into a wearable device. These calibration curves were used to accurately convert on-body sensor potential readings into Na^+ concentration measurements. For prepared Na^+ sensor batches with negligible sensor-to-sensor variation in voltage response, pre-calibration of every individual sensing unit was not necessary.

Author contributions

Z. Y., L. H., and M. B. conducted the experiments with assistance from other coauthors. Z. Y. and L. C. T. designed the device structure. Z. Y., L. H., H. Y. Y. N., and W. J. fabricated the sensor. L. L. provided help for data analysis. A. J. supervised the project. All authors contributed to the manuscript.

Conflicts of interest

The authors declare no competing financial interest.

Acknowledgements

This work was supported by the National Science Foundation (NSF) Nanomanufacturing Systems for Mobile Computing and Mobile Energy Technologies (NASCENT) and the Berkeley Sensor & Actuator Center (BSAC). The sensor fabrication was performed in the Electronic Materials (E-MAT) laboratory funded by the Director, Office of Science, Office of Basic Energy Sciences, Material Sciences and Engineering Division of the U.S. Department of Energy under Contract No. DE-AC02-05CH11231. The authors thank N. G. for her assistance with the illustrations and B. L. for helping with the experiment.

References

1 J. A. Rogers, T. Someya and Y. Huang, *Science*, 2010, **327**, 1603.
2 D.-H. Kim, J. Viventi, J. J. Amsden, J. Xiao, L. Vigeland, Y.-S. Kim, J. A. Blanco, B. Panilaitis, E. S. Frechette, D. Contreras, D. L. Kaplan, F. G. Omenetto, Y. Huang, K.-C. Hwang, M. R. Zakin, B. Litt and J. A. Rogers, *Nat. Mater.*, 2010, **9**, 511.
3 W. Gao, S. Emaminejad, H. Y. Y. Nyein, S. Challa, K. Chen, A. Peck, H. M. Fahad, H. Ota, H. Shiraki, D. Kiriya, D.-H. Lien, G. A. Brooks, R. W. Davis and A. Javey, *Nature*, 2016, **529**, 509.
4 H. Ota, K. Chen, Y. Lin, D. Kiriya, H. Shiraki, Z. Yu, T.-J. Ha and A. Javey, *Nat. Commun.*, 2014, **5**, 5032.
5 W. Gao, H. Y. Y. Nyein, Z. Shahpar, H. M. Fahad, K. Chen, S. Emaminejad, Y. Gao, L.-C. Tai, H. Ota, E. Wu, J. Bullock, Y. Zeng, D.-H. Lien and A. Javey, *ACS Sens.*, 2016, **1**, 866–874.
6 H. Y. Y. Nyein, W. Gao, Z. Shahpar, S. Emaminejad, S. Challa, K. Chen, H. M. Fahad, L.-C. Tai, H. Ota, R. W. Davis and A. Javey, *ACS Nano*, 2016, **10**, 7216–7224.
7 K. Chen, W. Gao, S. Emaminejad, D. Kiriya, H. Ota, H. Y. Y. Nyein, K. Takei and A. Javey, *Adv. Mater.*, 2016, **28**, 4397–4414.
8 K. Takei, W. Honda, S. Harada, T. Arie and S. Akita, *Adv. Healthcare Mater.*, 2015, **4**, 487–500.
9 H. Ota, S. Emaminejad, Y. Gao, A. Zhao, E. Wu, S. Challa, K. Chen, H. M. Fahad, A. K. Jha, D. Kiriya, W. Gao, H. Shiraki, K. Morioka, A. R. Ferguson, K. E. Healy, R. W. Davis and A. Javey, *Adv. Mater. Technol.*, 2016, **1**, 1600013.
10 G. Schwartz, B. C. K. Tee, J. Mei, A. L. Appleton, D. H. Kim, H. Wang and Z. Bao, *Nat. Commun.*, 2013, **4**, 1859.
11 A. Chortos, J. Liu and Z. Bao, *Nat. Mater.*, 2016, **15**, 937.
12 D.-H. Kim, N. Lu, R. Ma, Y.-S. Kim, R.-H. Kim, S. Wang, J. Wu, S. M. Won, H. Tao, A. Islam, K. J. Yu, T.-I. Kim, R. Chowdhury, M. Ying, L. Xu, M. Li, H.-J. Chung, H. Keum, M. McCormick, P. Liu, Y.-W. Zhang, F. G. Omenetto, Y. Huang, T. Coleman and J. A. Rogers, *Science*, 2011, **333**, 838.
13 S. Xu, Y. Zhang, L. Jia, K. E. Mathewson, K.-I. Jang, J. Kim, H. Fu, X. Huang, P. Chava, R. Wang, S. Bhole, L. Wang, Y. J. Na, Y. Guan, M. Flavin, Z. Han, Y. Huang and J. A. Rogers, *Science*, 2014, **344**, 70.
14 H. Y. Y. Nyein, L.-C. Tai, Q. P. Ngo, M. Chao, G. B. Zhang, W. Gao, M. Bariya, J. Bullock, H. Kim, H. M. Fahad and A. Javey, *ACS Sens.*, 2018, **3**, 944–952.

15 M. Bariya, Z. Shahpar, H. Park, J. Sun, Y. Jung, W. Gao, H. Y. Y. Nyein, T. S. Liaw, L.-C. Tai, Q. P. Ngo, M. Chao, Y. Zhao, M. Hettick, G. Cho and A. Javey, *ACS Nano*, 2018, **12**, 6978–6987.
16 M. Bariya, H. Y. Y. Nyein and A. Javey, *Nat. Electron.*, 2018, **1**, 160–171.
17 S. Setford, M. Grady, S. Mackintosh, R. Donald and B. Levy, *J. Diabetes Sci. Technol.*, 2018, **12**, 1016–1023.
18 L.-C. Tai, W. Gao, M. Chao, M. Bariya, Q. P. Ngo, Z. Shahpar, H. Y. Y. Nyein, H. Park, J. Sun, Y. Jung, E. Wu, H. M. Fahad, D.-H. Lien, H. Ota, G. Cho and A. Javey, *Adv. Mater.*, 2018, **30**, 1707442.
19 R. M. Morgan, M. J. Patterson and M. A. Nimmo, *Acta Physiol. Scand.*, 2004, **182**, 37–43.
20 S. I. Barr, *Can. J. Appl. Physiol.*, 1999, **24**, 164–172.
21 J. T. Korpelainen, K. A. Sotaniemi and V. V. Myllylä, *Neurology*, 1993, **43**, 1211.
22 J. Del Coso, C. González-Millán, J. J. Salinero, J. Abián-Vicén, F. Areces, M. Lledó, B. Lara, C. Gallo-Salazar and D. Ruiz-Vicente, *Scand. J. Med. Sci. Sports*, 2016, **26**, 156–164.
23 J. D. Coso, E. Estevez, R. A. Baquero and R. Mora-Rodriguez, *Appl. Physiol., Nutr., Metab.*, 2008, **33**, 290–298.
24 S. B. Kim, K. Lee, M. S. Raj, B. Lee, J. T. Reeder, J. Koo, A. Hourlier-Fargette, A. J. Bandodkar, S. M. Won, Y. Sekine, J. Choi, Y. Zhang, J. Yoon, B. H. Kim, Y. Yun, S. Lee, J. Shin, J. Kim, R. Ghaffari and J. A. Rogers, *Small*, 2018, **14**, 1802876.
25 L. E. Gibson and P. A. di Sant'Agnese, *J. Pediatr.*, 1963, **62**, 855–867.
26 H. M. Emrich, E. Stoll, B. Friolet, J. P. Colombo, R. Richterich and E. Rossi, *Pediatr. Res.*, 1968, **2**, 464–478.
27 Z. Sonner, E. Wilder, J. Heikenfeld, G. Kasting, F. Beyette, D. Swaile, F. Sherman, J. Joyce, J. Hagen, N. Kelley-Loughnane and R. Naik, *Biomicrofluidics*, 2015, **9**, 031301.
28 S. J. Montain, S. N. Cheuvront and H. C. Lukaski, *Int. J. Sport Nutr. Exercise Metab.*, 2007, **17**, 574–582.
29 A. J. Bandodkar, D. Molinnus, O. Mirza, T. Guinovart, J. R. Windmiller, G. Valdés-Ramírez, F. J. Andrade, M. J. Schöning and J. Wang, *Biosens. Bioelectron.*, 2014, **54**, 603–609.
30 B. Schazmann, D. Morris, C. Slater, S. Beirne, C. Fay, R. Reuveny, N. Moyna and D. Diamond, *Anal. Methods*, 2010, **2**, 342–348.